

Detection of New Galaxy Candidates at $z > 11$ in the JADES Field Using JWST NIRCам

Priyanka Chakraborty¹ ,  Arnab Sarkar² , Scott Wolk¹ , Benjamin Schneider² , Nancy Brickhouse¹ , Kenneth Lanzetta³, Adam Foster¹ , Randall Smith¹ 

¹Center for Astrophysics | Harvard & Smithsonian, Cambridge, MA 02138, USA

²Kavli Institute for Astrophysics and Space Research, Massachusetts Institute of Technology, 70 Vassar St, Cambridge, MA 02139

³Stony Brook University, Stony Brook, NY 11794-3800

Accepted XXX. Received YYY; in original form ZZZ

ABSTRACT

We report the detection of seven new galaxy candidates with redshift $z > 11$ within the JWST Advanced Deep Extragalactic Survey (JADES) GOODS-S and GOODS-N fields. These new candidates are detected through meticulous analysis of NIRCам photometry in eight filters spanning a wavelength range of 0.8–5.0 μm . Photometric redshifts of these galaxy candidates are independently measured utilizing spectral energy distribution (SED) fitting techniques using EAZY and BAGPIPES codes, followed by visual scrutiny. Two of these galaxy candidates are located in GOODS-S field, while the remaining five galaxies are located in GOODS-N field. Our analysis reveals that the stellar masses of these galaxies typically range from $\log M_*/M_\odot = 7.75\text{--}8.75$. Furthermore, these galaxies are typically young with their mass-weighted ages spanning from 80 to 240 Myr. Their specific star formation rates (sSFR), quantified as $\log(\text{sSFR}/\text{Gyr})$, are measured to vary between ~ 0.95 to 1.46. These new galaxy candidates offer a robust sample for probing the physical properties of galaxies within the first few hundred Myr of the history of the Universe. We also analyze the relationship between star formation rate (SFR) and stellar mass (M_*) within our sample. Using linear regression, our analysis yields a slope of 0.71 ± 0.12 , which we then compare with results from previous studies. Continued investigation through spectroscopic analysis using JWST/NIRSpec is needed to spectroscopically confirm these high-redshift galaxy candidates and investigate further into their physical properties. We plan to follow up on these candidates with future NIRSpec observations.

Key words: High-redshift galaxies – JWST

1 INTRODUCTION

The galaxies that emerged within the first few hundred million years after recombination are believed to have played a crucial role in shaping the early Universe by hosting its first stars. This first generation of stars initiated the process of ionizing neutral hydrogen throughout the cosmos. While reionization is generally understood to have occurred within the first billion years following the Big Bang, the precise mechanisms and the specific types of galaxies responsible for this phenomenon remain largely elusive and subject to ongoing debate (e.g., Barkana & Loeb 2001; Bromm & Larson 2004; Fan et al. 2006; Bromm & Yoshida 2011; Stark 2016; Ouchi et al. 2020). Thus, studying early galaxies is crucial for understanding their formation and evolution over billions of years, revealing insights into the physical processes that shaped them and their role in re-ionizing the Universe.

Over the past decade, deep surveys conducted by the Hubble Space Telescope (HST) discovered thousands of galaxies, significantly improving our understanding of the properties and demographics of

galaxies up to $z \sim 11$ (Ellis et al. 2013; Ishigaki et al. 2015; Finkelstein et al. 2015; McLeod et al. 2016; Bhatawdekar et al. 2019; Bouwens et al. 2021). These surveys included the Hubble Ultra-Deep Field (UDF, Beckwith et al. 2006), HUDF09 (Bouwens et al. 2011), HUDF12 (Ellis et al. 2013), the HST Great Observatories Origins Deep Survey (GOODS, Giavalisco et al. 2004), and many others (e.g., Scoville et al. 2007; Coe et al. 2019). However, the limited near-infrared (NIR) coverage of the HST, along with its moderate light-collecting capacity, limited the exploration of the evolution of galaxies at earlier ($z > 11$) epochs.

The method for selecting high-redshift galaxies has primarily been driven by photometry (Schenker et al. 2013; Bouwens et al. 2015). This technique exploits the absorption of ultraviolet light by neutral hydrogen within, around, and between distant galaxies. This absorption produces a distinctive spectral feature known as the “Lyman break,” observable at 912 Å in the spectral energy distribution (SED) of the galaxy (Sarkar & Samui 2019). The redshifts of these galaxies are determined by fitting their observed SEDs to either simulated or observed galaxy SEDs with known physical properties. This method incorporates more data than pure color selection alone (Bolzonella et al. 2000). To effectively apply this approach, accurate template

* E-mail: priyanka.chakraborty@cfa.harvard.edu

SEDs covering the entire color space of photometry are necessary, accounting for factors such as dust extinction and intergalactic medium (IGM) absorption. However, this procedure becomes less certain for high-redshift galaxies due to the scarcity of ultraviolet (UV) and optical SEDs for early galaxies (e.g., [Stark 2016](#)).

The commissioning of the James Webb Space Telescope (JWST) ([Rigby et al. 2023](#)) has opened a new window into the discovery and study of galaxies during the earliest stages of the universe, made possible by its improved sensitivity, $7\times$ light-collecting area, and the broad imaging field of NIRCam ([Rieke et al. 2005](#)). In the early months of operation, several $z > 11$ galaxy candidates were identified ([Naidu et al. 2022](#); [Finkelstein et al. 2022](#); [Harikane et al. 2023](#); [Donnan et al. 2023](#); [Atek et al. 2023a](#)) as part of JWST's Early Release Observations (ERO; [Pontoppidan et al. \(2022\)](#)), the Early Release Science (ERS) programs CEERS ([Bagley et al. 2023](#)) and Through the Looking GLASS (GLASS-JWST) programs ([Treu et al. 2022](#)). Many of the galaxy candidates identified in these early observations exceeded the previous distance record established by HST studies ([Oesch et al. 2016](#)). The discovery of early galaxy candidates has been further advanced by observational campaigns such as the JWST Advanced Deep Extragalactic Survey (JADES, [Eisenstein et al. 2023a](#)), the Next Generation Deep Extragalactic Exploratory Public (NGDEEP, [Austin et al. 2023](#)) survey, and the Prime Extragalactic Areas for Reionization and Lensing Science (PEARLS) project ([Windhorst et al. 2023](#); [Juodžbalis et al. 2023](#)), which have utilized photometric techniques to identify $z \sim 9$ -16 galaxy candidates.

JADES is one of the most extensive initiatives in JWST's first year of observation, dedicating 32 days of telescope time to the discovery and characterization of the most distant galaxies ([Rieke et al. 2023a](#)). The survey encompasses two deep fields, GOODS-South and GOODS-North, which have extensive legacy datasets provided by the Great Observatories Origins Deep Survey (GOODS; [Dickinson et al. 2003](#); [Giavalisco et al. 2004](#)), and utilizes three instruments: NIRCam for imaging, NIRSpec for spectroscopy, and MIRI with an imaging and spectroscopy. JADES operates at two levels of survey depth: "Deep" and "Medium." The Deep survey is designed for in-depth characterization of fainter galaxies or detailed analysis of individual sources at higher signal-to-noise ratios, whereas the Medium survey facilitates a statistical analysis of the high-redshift galaxy population.

In this paper, we report the detection of new $z > 11$ galaxy candidates using NIRCam observations taken across eight filters from the first year of the JADES survey in the GOODS-S and GOODS-N fields. We use two distinct codes EAZY ([Brammer et al. 2008](#)) and BAGPIPES ([Carnall et al. 2018](#)) for determining the redshifts of the candidates and their physical properties using SED fitting techniques to the photometric data. The format of the paper is as follows. In Section 2, we provide a detailed description of the observation and the photometric data reduction process, including photometric redshift estimation and dropout selection methods. In section 3, we detail the methodology for selecting galaxies at redshifts $z > 11$. In Section 4, we present the main results from our galaxy sample, including detailed descriptions, sizes, properties derived from SED fitting, and an analysis of systematic uncertainties and potential sources of contamination. In Section 5, we summarize our findings.

Throughout this paper, we adhere to the AB magnitude system ([Oke & Gunn 1983](#)) and cosmological parameters reported by [Planck Collaboration et al. \(2020\)](#): the Hubble constant $H_0 = 67.4 \text{ km s}^{-1} \text{ Mpc}^{-1}$, matter density parameter $\Omega_M = 0.315$, and dark energy density $\Omega_\Lambda = 0.685$.

2 OBSERVATION AND METHODS

The debut of the JWST in December 2021 opens up an unprecedented window into the study of the distant cosmos. Throughout the past year, a series of observation initiatives have been underway e.g., JADES ([Hainline et al. 2024](#)), CHEERS ([Finkelstein et al. 2015](#)), GLASS ([Castellano et al. 2022](#)), NGDEEP ([Leung et al. 2023](#)) and many others. This paper centers on the analysis of data stemming from the JADES programs, with a particular focus on photometry.

2.1 JADES GOODS-S and GOODS-N observations

In this study, we investigate galaxy candidates identified through NIRCam imaging within the GOODS-S and GOODS-N field. GOODS-S encompasses observations conducted under Program 1180 led by PI Eisenstein from UT 2022-09-29 to 2022-10-10 (e.g., [Bunker et al. 2023](#); [Eisenstein et al. 2023a](#); [Rieke et al. 2023b](#); [Eisenstein et al. 2023b](#)). Additionally, NIRCam parallels, covering 9.8 square arcminutes each, were observed during NIRSpec PID 1210 led by PI Ferruit from UT 2022-10-20 to 2022-10-24, positioned within and southwest of the JADES Medium footprint in GOODS-S. Further NIRCam observations (9.8 square arcminutes) parallel to NIRSpec PID 1286, also led by PI Ferruit, occurred from UT 2023-01-12 to 2023-01-13, situated northwest of the JADES Deep footprint in GOODS-S (e.g., [Robertson et al. 2023](#); [Tacchella et al. 2023](#); [Hainline et al. 2024](#)). The total survey area for JADES GOODS-S spans 67 square arcminutes, with 27 square arcminutes allocated for the JADES Deep program and 40 square arcminutes for the JADES Medium program. Utilizing filters F090W, F115W, F150W, F200W, F277W, F335M, F356W, F410M, and F444W ($\lambda = 0.8 - 5.0 \mu\text{m}$) for JADES Deep and the same filters without F335M for JADES Medium, these observations incorporate a minimum of six dither points per observation, with exposure times ranging from 14 to 60 ks. Consequently, the 5σ depths range from 3.4 to 5.9 nJy, with flux aperture sizes varying between 1.26 and 1.52 arcseconds.

The NIRCam GOODS-N program encompasses a total area of 58 square arcminutes. It's split into two sections: the northwest (NW) covering 30.4 square arcminutes, and the southeast (SE) covering 27.6 square arcminutes. The NW part was observed as part of PID 1181 (PI: Eisenstein), using NIRCam as the main instrument. JADES guarantees a high level of pixel diversity across all filter bands, effectively mitigating flat-field inaccuracies, cosmic-ray interference, and other pixel-level issues.

For this study, we utilized publicly available JADES data and reductions^{*}. We specifically used NIRCam images from eight filters: F090W, F115W, F150W, F200W, F277W, F356W, F410M, and F444W. These images were processed with a pixel scale of $0.03''$ per pixel. To identify sources in the images, we created a detection image by combining the F200W and F277W NIRCam bands using a weighted sum. We used image-segmentation tools from *Photutils* ([Bradley et al. 2023a](#)) and JWST data analysis tool notebooks[†] to identify sources with a SNR above 3 across five contiguous pixels. From this source catalog, we measured elliptical Kron aperture fluxes using *Photutils*. We used a flexible Kron scale factor ($K = 1.5$) and a circularized radius six times larger than the Gaussian-equivalent elliptical sizes to ensure accurate measurements while masking any segmentation regions of neighboring sources ([Bradley et al. 2023b](#); [Hainline et al. 2024](#)). The size of elliptical Kron aperture for each

^{*} <https://archive.stsci.edu/hlsp/jades>

[†] <https://jwst-docs.stsci.edu/jwst-post-pipeline-data-analysis>

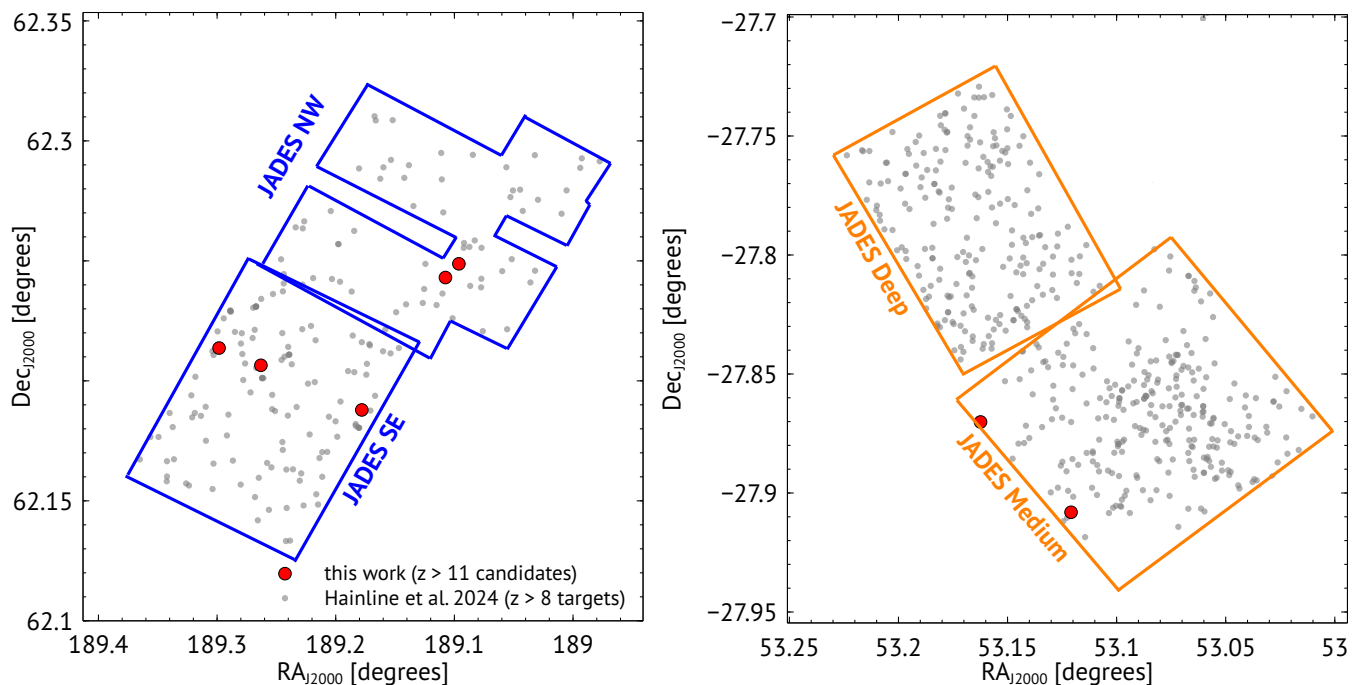


Figure 1. Left: Map displaying the GOODS-N field. The red data points represent our newly identified targets with $z > 11$ overlaid on the grey data points showing candidates with $z > 8$ listed in Hainline et al. (2024). Right: GOODS-S field. Our galaxy candidates with $z > 11$ were found in the JADES Medium GOODS-S region, with the grey data points again showing candidates with $z > 8$ from the same study.

source was estimated by multiplying the Kron scale factor by the individual Kron radius.

We extracted and fitted to SED for each source adopting the Kron fluxes, as previous studies have demonstrated that measuring colors in small elliptical apertures accurately captures the colors of distant galaxies (Finkelstein et al. 2023; Bradley et al. 2023b). Additionally, we repeated a similar analysis using Kron apertures with a scale factor of 2.5. To correct for aperture effects, we estimated an aperture correction by comparing the total fluxes measured in the larger and smaller apertures for each source. This correction factor was then applied to the fluxes and uncertainties for all filters.

2.2 Photometric redshift estimation

We used EAZY-py, the Python implementation of the EAZY photometric redshift estimator code (Brammer et al. 2008), to derive the initial photometric redshifts. We utilize a set of 12 “tweak_fps_QSF_12_v3 templates derived from the Flexible Stellar Population Synthesis (FSPS) library (Conroy et al. 2009; Conroy & Gunn 2010). These templates include a range of galaxy types including star-forming, quiescent, and dusty and also include a range of star-formation histories, e.g., bursty, slowly rising, and slowly falling. Additionally, we utilize six newly developed templates from Larson et al. (2023), which were also applied by Adams et al. (2024) for deriving photometric redshifts of galaxies with $z > 7.5$. These additional templates were found to provide better photometric redshift estimation for $z > 9$ galaxies.

We utilized the $\chi^2(z)$ values generated by EAZY to compute a probability distribution, $P(z)$, assuming a uniform redshift prior. This distribution is given by the equation $P(z) = \exp[\chi^2(z)/2]$, and it is normalized such that the integral of $P(z)$ over all redshifts equals 1.0. We vary redshifts in $0.1 < z < 20$, in steps of 0.01. Since the

high-redshift luminosity function is still not well-constrained, we adopted a flat luminosity prior to prevent bias against the selection of bright high-redshift galaxies. Similar techniques were also adopted in several past JWST studies, such as Finkelstein et al. (2022); Bradley et al. (2023b).

3 SELECTION CRITERIA FOR HIGH-REDSHIFT CANDIDATE

We selected high-redshift galaxy candidates by combining EAZY-based SED fitting for photometric redshifts, signal-to-noise (SNR) criteria, as adopted in several past studies such as Salmon et al. (2020); Finkelstein et al. (2022, 2023); Bradley et al. (2023b); Leung et al. (2023); Atek et al. (2023a); Donnan et al. (2023); Hainline et al. (2024). We adopted photometric SNR criteria to ensure nondetections in filters bluer than Ly α and robust detections in filters redder than Ly α break. Finally, we visually inspect each galaxy candidates for detector artifacts, diffraction spikes, and spurious noise close to detector edge.

Our selection criteria for identifying galaxy candidates with $z > 11$ are similar to the criteria adopted in Finkelstein et al. (2022) and Bradley et al. (2023b)-

- (i) The candidates should be newly discovered and have not been detected in any previous JWST studies.
- (ii) The best-fit photometric redshift, derived from EAZY SED fitting, must exceed 11 (i.e., $z > 11$).
- (iii) An SNR of < 1.5 to ensure non-detections blueward of Lyman- α in all of the following filters F090W and F115W for $z < 13$. An additional F150W SNR of < 1.5 was also adopted for $z \geq 13$.
- (iv) An SNR > 5.5 in at least two of the following filters: F150W,

F200W, F277W, F356W, F410M, or F444W for $z < 13$ and F200W, F277W, F356W, F410M, or F444W for $z > 13$.

(v) The integral of the EAZY posterior redshift probability ($P(z)$) of the galaxy being at $z > 11$ is greater than 70%, i.e. $\int_{z=11}^{\infty} P(z) dz > 0.7$.

(vi) The angular separation between the candidates and any other nearby bright sources are at least $0.3''$, corresponding to 10 pixels.

In addition to the above criteria, we fitted each SED twice, first restricting EAZY maximum redshift to $z < 7$ (low-redshift) and then varying the redshift between $0 < z < 20$ (high redshift). We estimated the disparity between the best-fit χ^2 for the low-redshift and high-redshift fit. For this work, we only consider $\Delta\chi^2 \geq 9$, ruling out the low-redshift model at $\geq 3\sigma$ significance (Harikane et al. 2023).

4 RESULTS AND DISCUSSION

Adopting the selection criteria and SED fitting method, we detect seven new galaxy candidates at redshift $z > 11$ in the JADES GOODS-S and GOODS-N field. Below we discuss our primary results.

4.1 Galaxy sample with $z > 11$

Utilizing fits generated by EAZY-py and BAGPIPES, we identify seven new candidates within the redshift range of $11 < z < 15$ across the GOODS-S and GOODS-N fields. Specifically, the five candidates are detected in GOODS-N, with the remaining two candidates detected in the GOODS-S field. Among the five candidates in GOODS-N, three are located in the southeastern sector, while the remaining two are located in its northwestern region. The two targets found in the GOODS-S field are specifically located within its medium region. Figure 1 illustrates the positions of these candidates in the GOODS-N and GOODS-S fields. Among the seven candidates, three had redshifts between 11 and 12, while the remaining four showed best-fit photometric redshifts exceeding 12. Table 1 lists the newly identified candidates along with best-fit parameters from SED fitting.

All candidates are robust detections characterized by a precise high-redshift solution without any significant competing low-redshift alternatives, with ~ 70 -100% of their total probability concentrated within $\Delta z = 1$ around the best-fit solution. Similar quality classification criteria have been adopted in a recent *JWST* UNCOVER high-redshift survey (Atek et al. 2023b), where candidates meeting such criteria have been labeled as high-quality. Our sample targets the faint end of the luminosity distribution, covering a magnitude range of $m_{F277W} = 28.5$ and 30.4. Previous JADES surveys have documented systems with F277W AB magnitudes reaching as faint as 31.0 (Hainline et al. 2024). Figure 2, 3, 4, 5, 6, 7, and 8 shows the $1.8'' \times 1.8''$ thumbnail images, best-fit SED from BAGPIPES fit, and the posterior redshift distributions. The red points represent the measured photometry. The best-fit favored high-redshift solutions (represented by blue lines) have been shown along with the best-fit low-redshift solutions (represented by grey lines). The SED modeling and the physical properties of the galaxies derived from BAGPIPES fits are described in Section 4.3.

In our dataset, we identified three targets within the lowest redshift range in our sample, $11 < z < 12$ (EAZY determined), as illustrated in Figure 2, 3, and 4: JADES-53.16238-27.87016 (GOODS-S), JADES- 189.17805+62.18788 (GOODS-N), and JADES- 189.09621+62.24877 (GOODS-N). In the observed $11 < z < 12$ galaxies, none exhibit substantial flux in the

F115W images, thus classifying them as F115W dropout candidates. In the next higher redshift range, our survey identified 4 candidate galaxies with photometric redshifts $12 < z < 15$ (EAZY determined): JADES-53.12089-27.90810 (GOOD-S), JADES- 189.26307+62.20648 (GOODS-N), JADES- 189.29834 +62.21367 (GOODS-N), and JADES- 189.10753+62.24305 (GOODS-N). The corresponding thumbnail images are displayed in Figure 5, 6, and 7. JADES- 53.12089 -27.90810 is identified as an F150W dropout, while JADES- 189.26307+62.20648 is categorized as an F115W dropout. The $z \geq 13$ targets, JADES- 189.29834+62.21367 and JADES- 189.10753 +62.24305 are both categorized as F150W dropouts.

4.2 Size of galaxies

We estimated the sizes of all 7 galaxies in our sample through the parametric fitting of the NIRCam images using the Python package Photutils, an Astropy package for photometry and detection of astronomical sources (Bradley et al. 2022). We estimated the half-light radius for F277W filter using the Kron scale factor of 2.5, as adopted by Bradley et al. (2023b).

In Figure 9, we present the F277W half-light radii of our high-redshift galaxy candidates. The figure displays both the pixel size and the corresponding physical sizes (in kpc). The physical sizes were estimated using the photometric redshifts derived from BAGPIPES fits, as shown in Table 1. We find half-light radii ranging between 2.0 pixels to 2.7 pixels, corresponding to an angular spread between $0.06''$ and $0.081''$ (adopting pixel size of $0.03''$), with a median of $0.063''$. Given the F277W PSF full-width at half maximum of $0.088''$, and a radius of $0.044''$, all the galaxies are spatially resolved. The angular spreads translate to half-light radii ranging between 0.24 kpc to 0.34 kpc, with a median of 0.25 kpc for our galaxy candidates. These dimensions are in agreement with the rest-UV sizes reported in the GLASS survey, indicating a median half-light radius of 0.45 ± 0.13 kpc for $7 < z < 15$ galaxies in the F444W band (Yang et al. 2022), as well as with the CEERS survey, which found a median half-light radius of 0.46 kpc for $9 < z < 16$ galaxies in the F200W band (Finkelstein et al. 2023).

4.3 Physical Properties through SED fitting

To derive the physical properties of the identified galaxy candidates, we utilized the state-of-the-art Bayesian SED fitting code BAGPIPES (Carnall et al. 2018) to fit the observed SED. BAGPIPES generates complex model galaxy spectra and fits photometric and spectroscopic observations using the MultiNest nested sampling algorithm (Feroz & Hobson 2008), thereby generating posterior distributions of galaxy properties for each source in the sample. BAGPIPES is capable of modeling galaxies with various star formation histories (SFHs), including delayed- τ , constant, and bursts (Lower et al. 2020). The stellar population synthesis models adopted for this work are based on BC03 (Bruzual & Charlot 2003) version 2016. These models assume the Kroupa (2002) initial mass function (IMF) and include nebular line and continuum emission using CLOUDY (Chatzikos et al. 2023). For this study, we selected a delayed- τ SFH (where $\text{SFR}(t) \propto t \exp(-t/\tau)$), known for its effectiveness in modeling the majority of the stellar population and accurately estimating stellar masses (Ciesla et al. 2017).

We modified the BAGPIPES source code to expand the default redshift range from $z = 0-10$ to $z = 0-20$, ensuring consistency with the EAZY-py results used to select the galaxy sample (Section

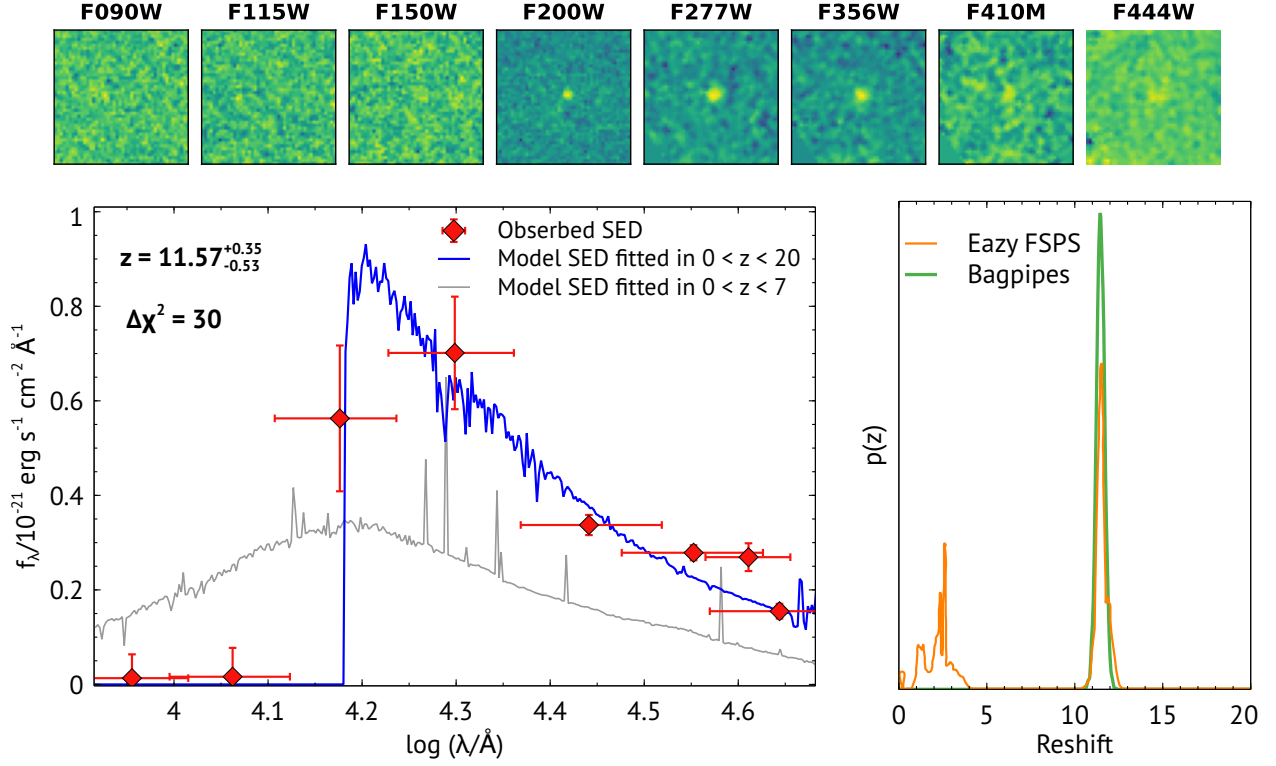


Figure 2. Thumbnail images for JADES- 53.16238 -27.87016. In each panel, the top rows display $1.8'' \times 1.8''$ image cutouts for the 8 JWST filters. The bottom-left panels represent the observed photometry in red data points along with their corresponding 1σ uncertainties. The best-fit SEDs with BAGPIPES for the preferred high-redshift solution are shown with blue curves, while the SEDs corresponding to the low-redshift solution are represented by grey curves. The redshift range displayed in the plot was determined using EAZY. In addition, the posterior probability distributions, $P(z)$, for photometric redshift solutions is displayed with the orange curves in the bottom-right panels.

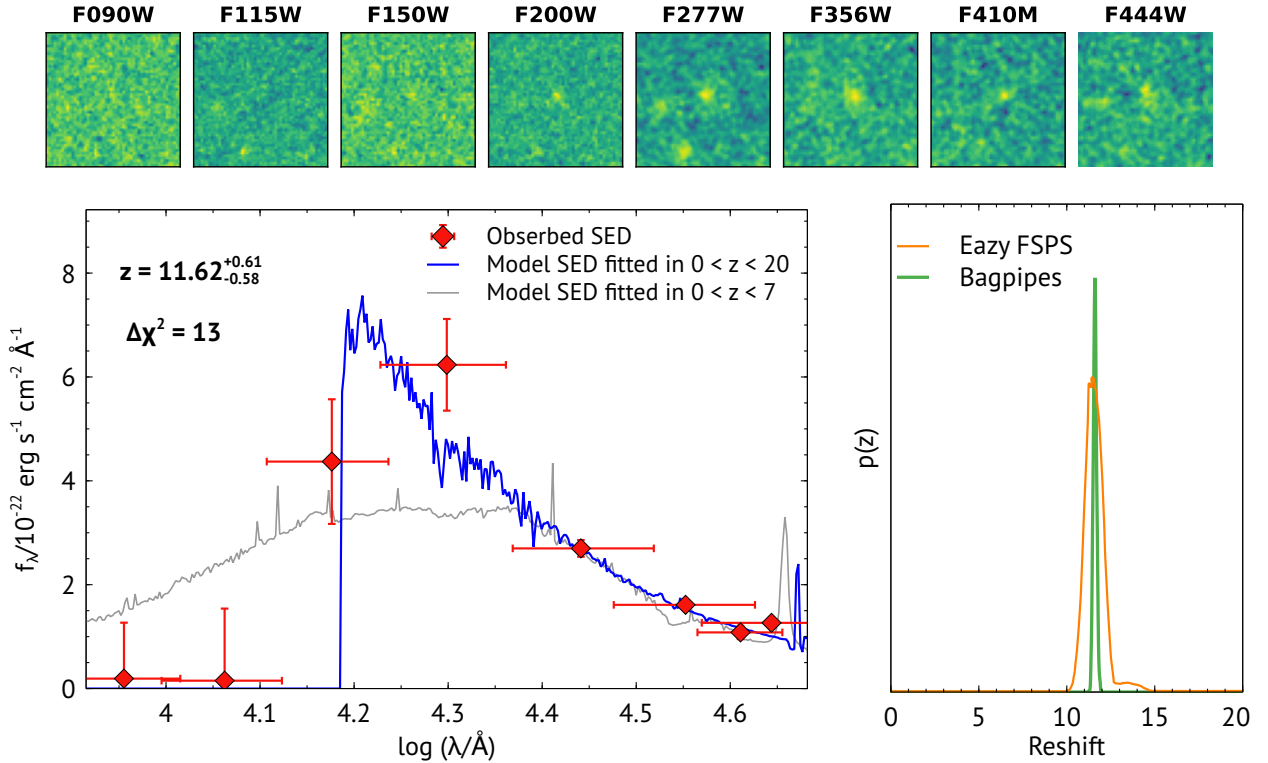


Figure 3. Same as Figure 2, but for JADES- 189.17805+62.18788.

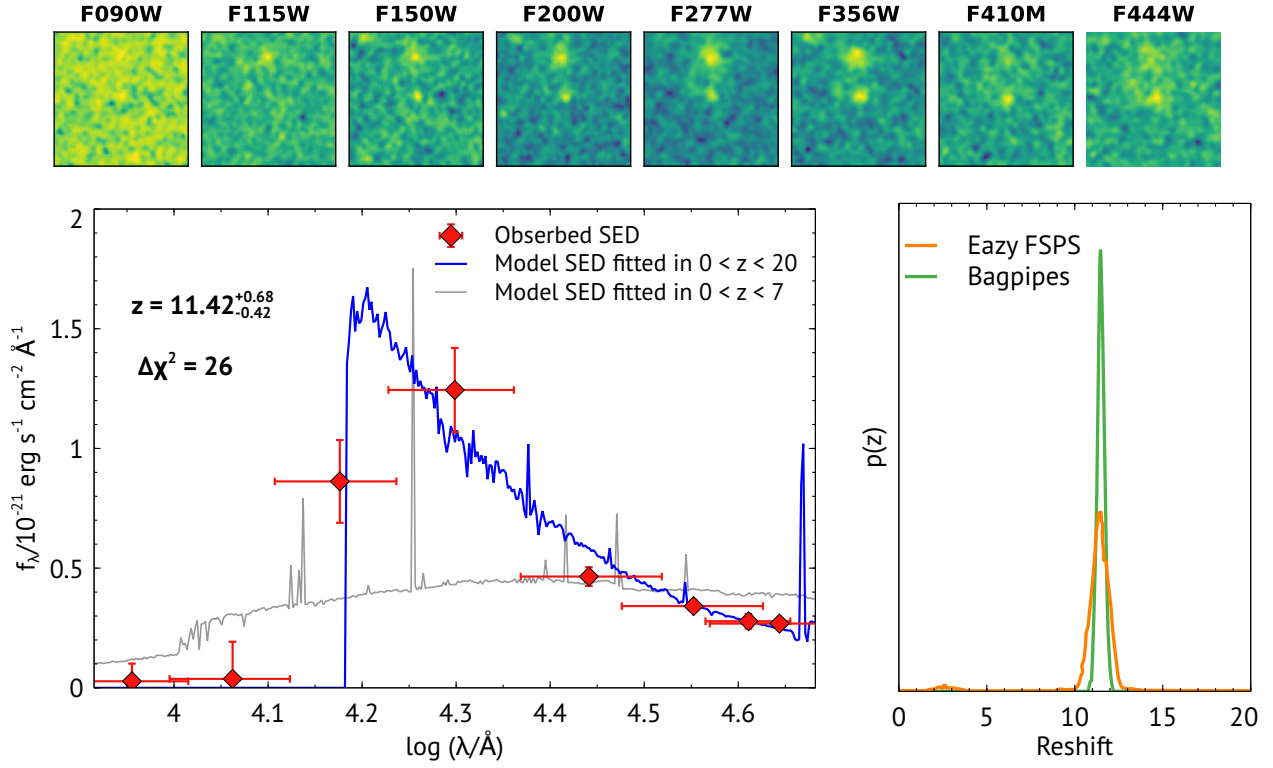


Figure 4. Same as Figure 2, JADES- 189.09621+62.24877

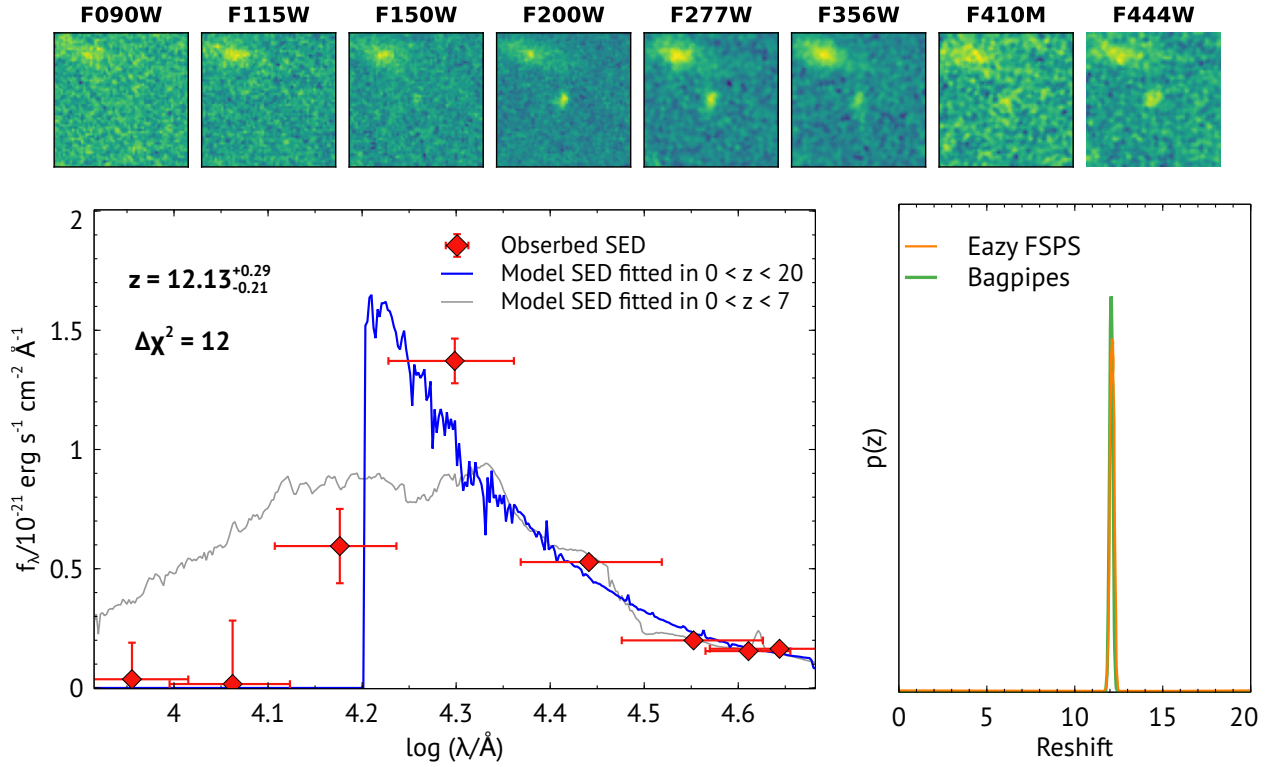


Figure 5. Same as Figure 2, but for JADES- 53.12089 -27.90810.

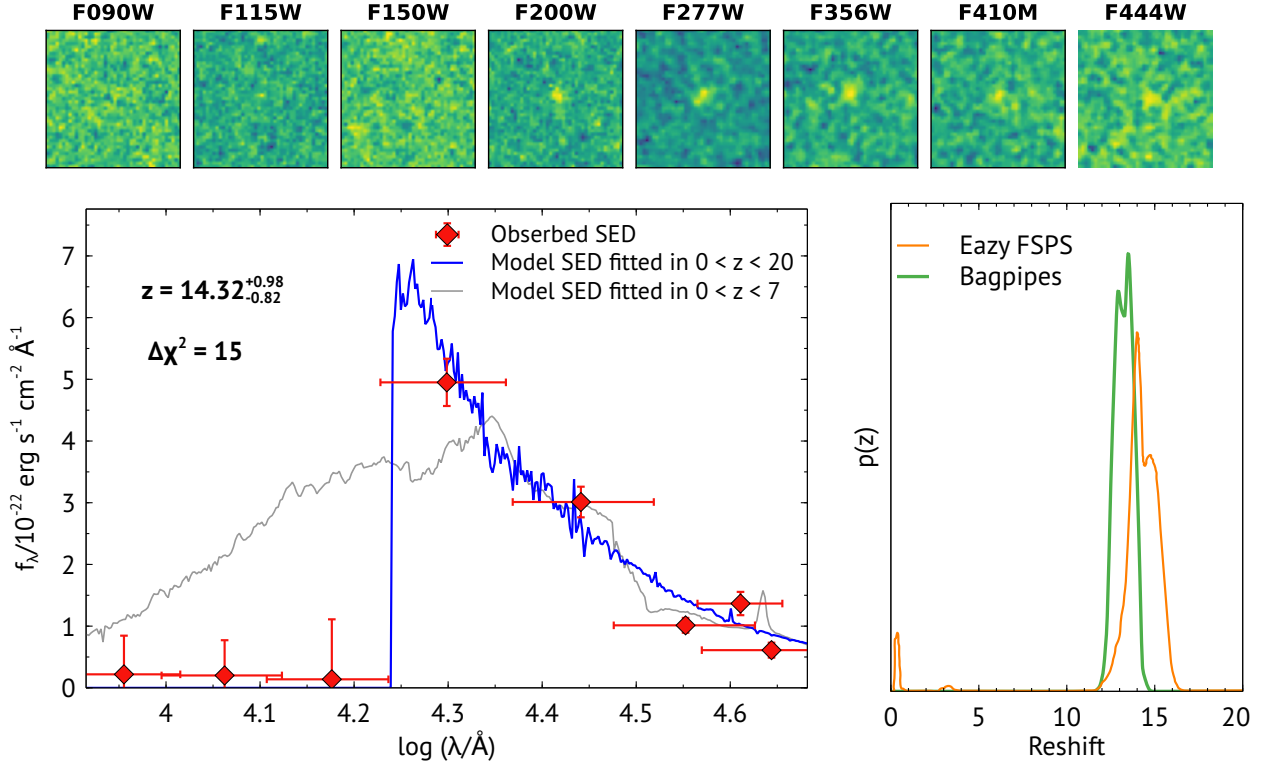


Figure 6. Same as Figure 2, but for JADES- 189.29834 +62.21367

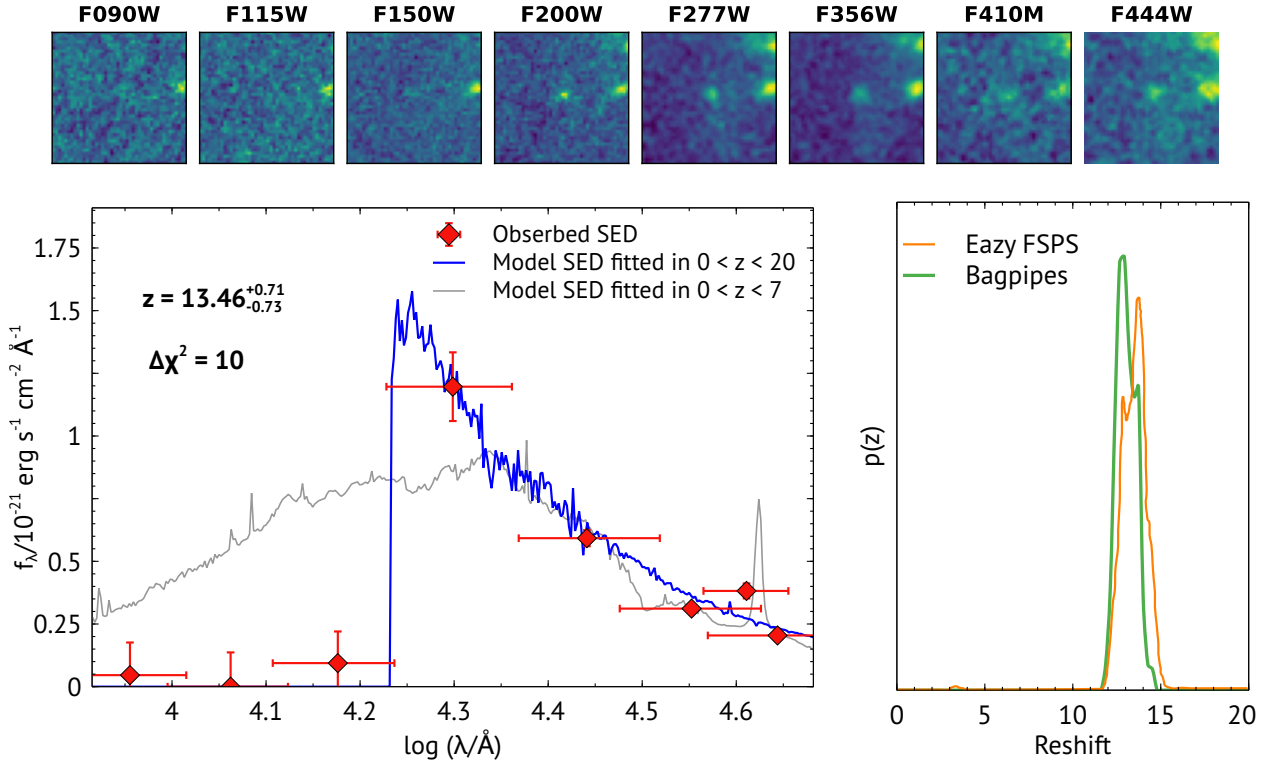


Figure 7. Same as Figure 2, but for JADES- 189.10753+62.24305.

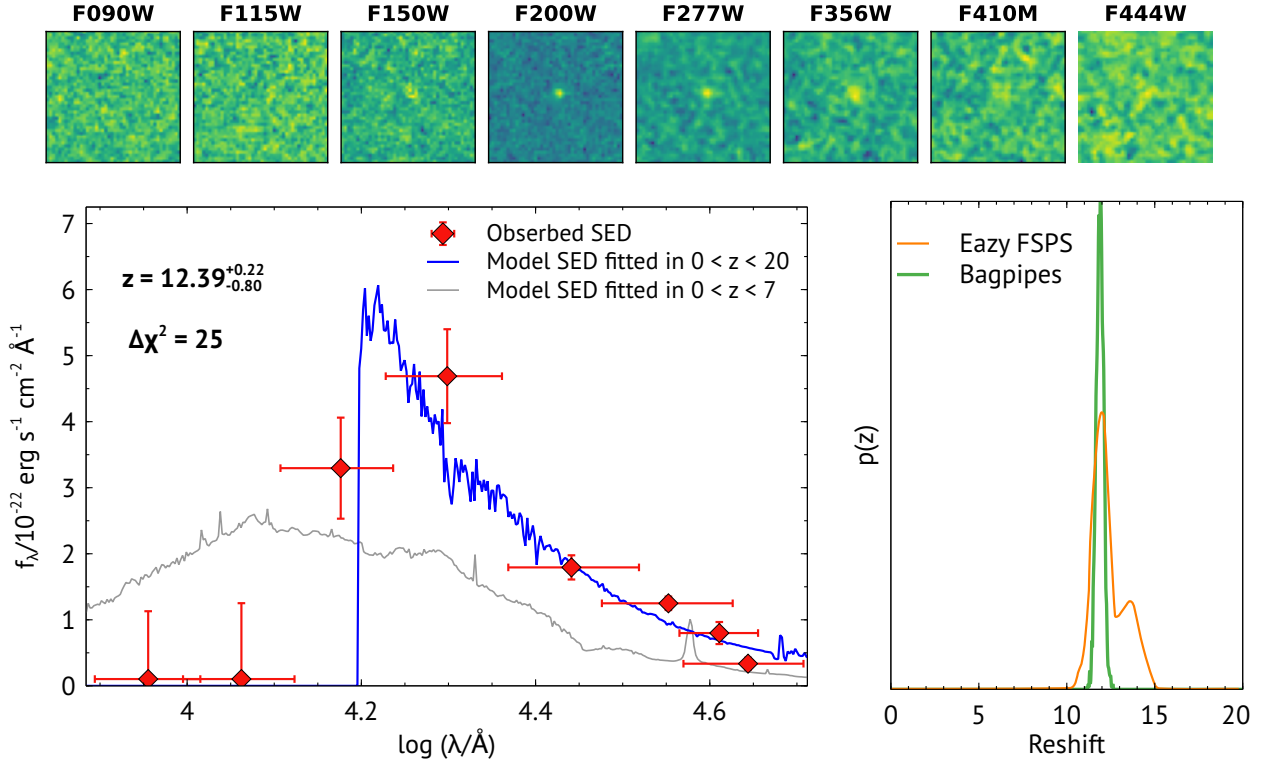


Figure 8. Same as Figure 2, but for JADES– 189.26307+62.20648.

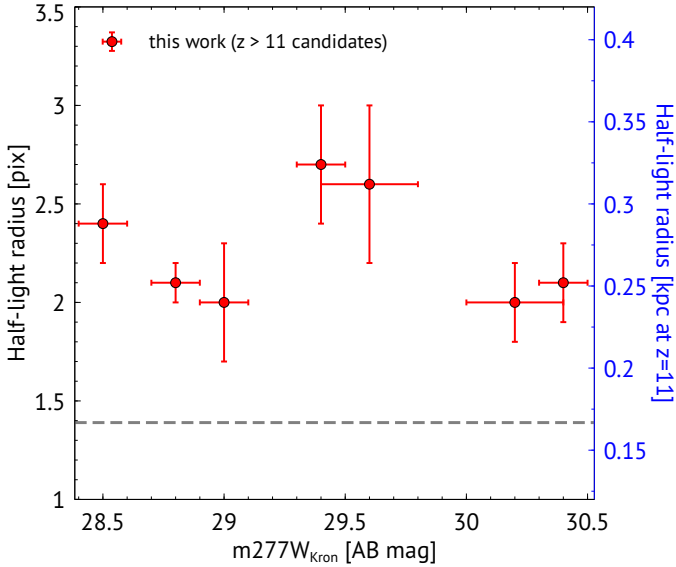


Figure 9. Half-light radius vs. AB Kron magnitude in F277W filter. Red data points show the Half-light radius of our sample galaxy candidates with 1σ uncertainties. A secondary y-axis for half-light radius in kpc (scaled at $z = 11$) is shown on the right side. The grey dashed line displays the F277W PSF FWHM in pixels (1.397 pixels).

2.2). The BAGPIPES SED-fitting was conducted over a wide range of parameter space. We vary τ within 0.1 and 14 Gyr, stellar masses within $\log(M_*/M_\odot) = 4$ and 13, and log of metallicities ($\log Z/Z_\odot$) within 0.005 and 2.5. The logarithm of the ionization parameter ($\log U$), for accounting nebular line and continuum emission, was allowed to vary within -4 and -2 . For this work we adopted Calzetti dust

attenuation curve to reduce the number of free parameters in our fits (Calzetti et al. 2000). We let the dust extinction A_V vary within 0 and 4. Additionally, we introduced a multiplicative factor ($1 < \eta < 2$) to the dust model to address birth-cloud dust attenuation, which typically doubles around H II regions compared to the general ISM within the galaxy’s first 10 Myr (Bradley et al. 2023b). To account for this, we capped the maximum age of the birth-cloud at 0.01 Gyr (Giménez-Arteaga et al. 2023). The age parameter was allowed to range from 1 Myr to the age of the Universe. Following a similar approach to the EAZY fitting, we conducted two fits of the observed photometry with BAGPIPES. Initially, we constrained the redshift range to $z < 7$. Then, we performed another fitting while allowing the redshift to vary between 0.1 and 20. Figure 2, 3, 4, 5, 6, 7, and 8 display the best-fit model SEDs obtained from the BAGPIPES fitting, accompanied by the corresponding $\Delta\chi^2$ values.

The physical parameters extracted from the BAGPIPES fittings are detailed in Table 1. Among these parameters, the inferred intrinsic stellar masses exhibit a range approximately from $\log M_*/M_\odot \sim 7.75$ to 8.75, while the corresponding star formation rates (SFRs) span from around ~ 0.9 to $5.1 M_\odot/\text{yr}$. Additionally, the specific star formation rates (sSFRs), quantified as $\log \text{sSFR}/\text{Gyr}$, vary within the range of approximately ~ 0.95 to 1.46. Notably, analogous sSFRs have been documented for galaxy candidates at redshifts $z > 8$ in Bradley et al. (2023b).

Furthermore, the inferred ages for all galaxy candidates within our sample indicate younger stellar populations, spanning a range of approximately 80 to 240 million years, similar to the ages found in earlier photometric detections of galaxies at $z \sim 10$ (Laporte et al. 2021; Bradley et al. 2023b). Regarding dust extinction, the best-fit values of A_V range from 0.02 to 0.45. These values are consistent with those found in $z = 9 - 16$ galaxies in the NGDEEP survey (Morales et al. 2024), which were also fitted using BAGPIPES and

Table 1. Photometric redshifts from EAZY and BAGPIPES, along with physical properties of the galaxy candidates estimated with BAGPIPES. Errors are estimated with 1σ uncertainties.

RA (deg)	DEC (deg)	z_{EAZY}	z_{Bagpipes}	m_{F277} (AB mag)	$\Delta\chi^2$ (68%)	$P(z)$	$\log(M_*/M_\odot)$	SFR ($M_\odot\text{yr}^{-1}$)	Age (Myr)	A_V	r_{hl} (pix/arcsec)
GOODS-S											
53.16238	-27.87016	$11.57^{+0.35}_{-0.53}$	$11.46^{+0.24}_{-0.23}$	28.8 ± 0.1	30	0.7	$8.59^{+0.19}_{-0.29}$	$4.2^{+2.2}_{-1.1}$	200^{+130}_{-120}	$0.45^{+0.15}_{-0.15}$	2.1 ± 0.1
53.12089	-27.90810	$12.13^{+0.29}_{-0.21}$	$12.07^{+0.09}_{-0.09}$	28.5 ± 0.1	12	1.0	$7.94^{+0.37}_{-0.60}$	$2.5^{+1.5}_{-0.5}$	80^{+150}_{-80}	$0.02^{+0.02}_{-0.01}$	2.4 ± 0.2
GOODS-N											
189.17805	62.18788	$11.62^{+0.61}_{-0.58}$	$11.5^{+0.1}_{-0.1}$	30.4 ± 0.1	13	0.9	$8.25^{+0.17}_{-0.27}$	$1.8^{+0.7}_{-0.3}$	230^{+100}_{-140}	$0.22^{+0.12}_{-0.11}$	2.1 ± 0.2
189.26307	62.20648	$12.39^{+0.22}_{-0.80}$	$11.89^{+0.20}_{-0.22}$	29.0 ± 0.1	25	0.9	$7.75^{+0.26}_{-0.31}$	$0.9^{+0.2}_{-0.2}$	120^{+80}_{-70}	$0.10^{+0.07}_{-0.03}$	2.0 ± 0.3
189.29834	62.21367	$14.32^{+0.98}_{-0.82}$	$13.5^{+0.5}_{-0.6}$	30.2 ± 0.2	15	0.9	$7.93^{+0.23}_{-0.45}$	$1.3^{+0.3}_{-0.3}$	136^{+120}_{-100}	$0.06^{+0.08}_{-0.04}$	2.0 ± 0.2
189.10753	62.24305	$13.46^{+0.71}_{-0.73}$	$13.01^{+0.65}_{-0.52}$	29.4 ± 0.1	10	0.9	$8.62^{+0.12}_{-0.20}$	$4.2^{+1.3}_{-0.7}$	190^{+90}_{-80}	$0.23^{+0.09}_{-0.10}$	2.7 ± 0.3
189.09621	62.24877	$11.42^{+0.68}_{-0.42}$	$11.5^{+0.2}_{-0.2}$	29.6 ± 0.2	26	0.9	$8.75^{+0.17}_{-0.25}$	$5.1^{+2.2}_{-1.2}$	240^{+100}_{-140}	$0.40^{+0.15}_{-0.13}$	2.6 ± 0.4

exhibited A_V values between 0.04 and 1.03. These findings collectively contribute to a deeper understanding of the stellar populations and dust properties within the observed galaxy sample.

4.4 SFR vs. stellar mass relation

Noeske et al. (2007) and Elbaz et al. (2007) demonstrated that galaxies at $z \sim 1$ exhibit a tight correlation between star formation rate and stellar mass, with a scatter of 0.2 dex and a rough proportionality characterized by a logarithmic slope of 0.9. This proportionality is similarly observed at $z \sim 0$ using data from the Sloan Digital Sky Survey (Elbaz et al. 2007). However, the normalization at $z \sim 0$ is lower, reflecting the overall decline in cosmic star formation rate density over time. This tight correlation between SFR and stellar mass, known as the main sequence (MS) of star formation, has been extensively documented in the literature (e.g., Daddi et al. 2007; Noeske et al. 2007; Elbaz et al. 2007). This relationship has been observed in high redshifts, with its evolution parametrized up to $z \sim 6$ (e.g., Speagle et al. 2014). However, establishing the MS at high redshifts poses significant challenges due to various systematic uncertainties and selection effects inherent in compiling representative galaxy samples (e.g., Grazian et al. 2015; Förster Schreiber & Wuyts 2020; Furtak et al. 2021, 2023). In order to probe the poorly understood Universe at $z \gtrsim 10$, which is beginning to unfold with the advent of the JWST, we investigate the SFR–stellar mass (SFR– M_*) relation within our sample and compare it with previous studies.

In Figure 10, we present the distribution of our galaxy sample in the SFR– M_* plane, derived using BAGPIPES with a 100 Myr SFR time-scale (as described in Section 4.3). We compare our findings with datasets from the NGDEEP survey for $z = 9$ –16 galaxies (Morales et al. 2024), CEERS for $z = 3$ –10 galaxies (Nakajima et al. 2023), earlier JADES surveys for $z = 3$ –10 galaxies (Curti et al. 2024), and the main sequence of star-forming galaxies at $z \sim 6$ (Salmon et al. 2015; Popesso et al. 2023). Our results closely align with those of established studies. Moreover, when fitting the stellar mass versus SFR for our seven galaxy candidates using linear regression, we obtain a slope of 0.71 ± 0.12 , as depicted in Figure 10. Although

the slope of our best-fitting line appears less steep compared to those reported in the aforementioned studies, it is important to acknowledge that this discrepancy could stem from biases in our sample selection.

4.5 Limitations of SED-fitting method and contaminations

We solely utilize SED fitting tool BAGPIPES to derive the physical properties of our high-redshift sample of galaxies. Though the effectiveness and flexibility of BAGPIPES code has been shown in many previous studies, such as Bradley et al. (2023b); Morales et al. (2024), the physical properties of high-redshift galaxies derived from BAGPIPES may be affected by several limitations and contaminations.

Analyzing SEDs through fitting broadband photometry, which mainly captures the rest-frame UV emissions of potential high-redshift galaxies is one of the limitations of our analysis. This wavelength range primarily highlights massive, short-lived stars within a galaxy, which might not represent the majority of its stellar mass. Due to the limited availability of rest-frame optical photometry, SED fitting is expected to underestimate stellar masses. Specifically, Furtak et al. (2021) demonstrated that relying solely on UV photometry can result in an underestimation of stellar masses by up to 0.6 dex. Stellar masses can be accurately derived from the UV continuum only if a galaxy is $\lesssim 10$ Myr old, which is the typical lifetime of massive stars. Beyond this age, accurate stellar mass determination requires continuum detection redward of the Balmer break. Furthermore, relying solely on rest-frame UV photometry can create ambiguities between stellar mass, SFR, and age, as noted by Furtak et al. (2023). To confirm if galaxies at $z \gtrsim 10$ possess an evolved stellar population, as suggested by recent simulations (Mason et al. 2023), JWST/NIRCam imaging at wavelengths $\lambda \leq 5\mu\text{m}$ should be supplemented with deep imaging from the Mid-Infrared Instrument (MIRI). This approach will enable the probing of the rest-frame optical emission of these very high-redshift galaxies.

Another constraint of our analysis arises from assuming a Lyman continuum (LyC) escape fraction of $f_{\text{esc}} = 0$ as per BAGPIPES. However, the LyC escape fraction significantly influences the shape of the SED through its impact on nebular emission. Specifically, it at-

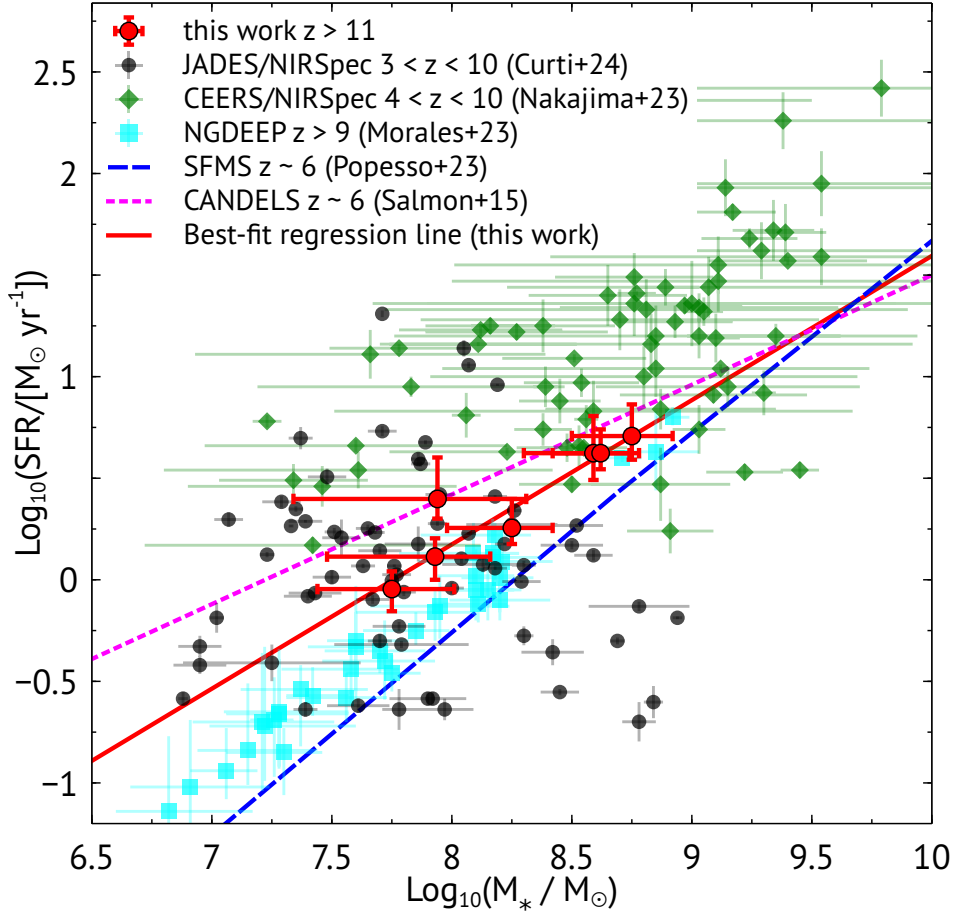


Figure 10. The distribution of stellar mass versus star-formation rate for our photometric galaxy sample is shown, incorporating data from CEERS (Nakajima et al. 2023), JADES (Curti et al. 2024), and NGDEEP (Morales et al. 2024). The new galaxy candidates identified in this study are represented by red circles. The red solid line represents the best-fit regression line derived from fitting our galaxy sample. Black circles indicate JADES/NIRSpec-selected galaxies spanning a redshift range of $3 < z < 10$, as presented in Curti et al. (2024), derived from both PRISM spectra and NIRCAM photometry. CEERS galaxies, shown as green diamonds, have their star-formation rates (SFRs) compiled from Nakajima et al. (2023), inferred from $H\beta$ luminosity. NGDEEP galaxies, marked in cyan, have their SFRs derived from photometry (Morales et al. 2024). The main sequence of star-forming galaxies at $z \sim 6$ from Popesso et al. (2023) and Salmon et al. (2015) are depicted by blue dashed and magenta dotted lines, respectively.

tenuates both nebular line and continuum emissions, resulting in a bluer SED and a steeper UV slope (Plat et al. 2019). Observations of known LyC leakers at low redshifts reveal a clear correlation between UV slope and LyC escape fraction (Chisholm et al. 2022). Although recent studies suggest low $f_{\text{esc}}(\text{LyC})$ values of $\lesssim 10\%$ in galaxies at $z > 7$ (Witten et al. 2023), it remains essential to account for the effect of $f_{\text{esc}}(\text{LyC})$ in highly star-forming primeval galaxies in the early Universe. This consideration is paramount as it could pose challenges in replicating the extremely blue UV slopes observed in some galaxies detected by JWST at $z > 10$. Therefore, future investigations aimed at accurately determining physical parameters of high-redshift galaxies through SED-fitting must incorporate templates that allow for $f_{\text{esc}} > 0$.

The primary source of contamination in broad-band photometry of high-redshift galaxy samples often stems from low-mass Milky Way stars and brown dwarfs. These celestial objects, especially at low temperatures, can exhibit near-infrared (near-IR) colors akin to those of high-redshift galaxies. Previous studies utilizing the HST have indicated that dropout selection techniques can yield contamination levels of up to 40% from low-redshift sources (Bouwens et al. 2011). Hence, it is imperative to consider this possibility in our

analyses. Numerous investigations have delved into the identification of these sources within extragalactic surveys (e.g., Finkelstein et al. 2015; Hainline et al. 2020). Brown dwarf candidates have been identified in extragalactic surveys such as GLASS (Nonino et al. 2023). However, the majority of these candidates remain unresolved owing to the relatively large near-infrared camera (NIRCcam) point spread function (PSF) of approximately $0.063''$ for longer wavelengths ($> 2\mu\text{m}$). We assess our results to gauge the potential for low-redshift contaminations.

Following previous studies, such as, those by Bradley et al. (2023b) and Furtak et al. (2023), we extend our analysis by fitting observed SEDs using both EAZY and BAGPIPES. In this process, redshifts were systematically varied within the range of $z < 7$ to bias the photometric redshift solutions towards lower values. For all seven galaxies within our sample, the low-redshift fits yield significantly lower significance (i.e., $\Delta\chi^2 > 9$) when compared to their corresponding high-redshift solutions. Moreover, it is noteworthy that all galaxies in our sample are well-resolved in the NIRCcam longer wavelength channel, with a half-light radius exceeding $0.06''$ at the F277W band. This observation effectively dismisses the possibility that the galaxies in our sample are low-mass Milky Way stars or brown dwarfs.

Although our selection criteria for high-redshift samples are meticulously crafted to mitigate contamination from lower-redshift interlopers, the potential still exists for some of our candidates to reside at lower redshifts. Spectroscopic confirmation is imperative to accurately determine the redshifts of these candidates.

5 CONCLUSION

In this paper, we present the outcomes of our investigation aimed at identifying $z > 11$ galaxy candidates in the JWST NIRCam observations of JADES GOODS-S and GOODS-N fields. We undertake an extensive data reduction process that involves several custom procedures. We use two distinct codes, EAZY and BAGPIPES, for photometric redshift determination and investigating the properties of these galaxies. We detect seven $z > 11$ candidate galaxies distributed as follows: three candidates between $11 < z < 12$, and four candidates between $12 < z < 15$. All candidates are robust high-redshift detections with 70–100% of their probability within $\Delta z = 1$, meeting the classification ‘high-quality’ used in a recent JWST UNCOVER high-redshift survey (Atek et al. 2023b). The detection of these young galaxies spans a diverse range of magnitudes, with F277W AB Kron magnitude values between 28.5 and 30.4, consistent with previous JADES surveys, which achieved detections as faint as AB mag 31.0 for the young galaxies at redshifts greater than 10 (Hainline et al. 2024).

To assess the physical properties of the galaxies, we perform SED fitting to the photometric data of these galaxies using BAGPIPES. We obtain measurements for stellar mass, SFRs averaged over the last 100 Myr, specific star sSFR, dust content, and mass-weighted age, which are documented in Table 1. We find the intrinsic stellar masses of our galaxy candidates to vary within the range of $\log(M_*/M_\odot) = 7.75$ to 8.75. Their SFRs span between 0.9 and $5.1 M_\odot \text{yr}^{-1}$, while their sSFRs, quantified as $\log \text{sSFR/Gyr}$, range from 0.95 to 1.46. The mass-weighted ages of these galaxies range between 80 to 240 Myr, with their dust content varying between $A_V = 0.02$ and 0.45. We present the distribution of galaxy candidates on the stellar mass versus star formation rate plane and compare our findings, which closely align with those of previous surveys (Nakajima et al. 2023; Morales et al. 2024; Curti et al. 2024).

Previous studies have demonstrated that photometry is a reliable method for determining galaxy properties. When used in conjunction with SED fitting codes such as BAGPIPES, photometry can reliably estimate photometric redshifts, stellar masses, and star formation rates (Duan et al. 2024). However, slight differences that may arise between properties derived from spectroscopy and those obtained through photometry must be considered when calibrating an absolute scale for the star formation rates and stellar mass histories of galaxies. Moving forward, JWST/NIRSpec observations will be essential for confirming these early galaxies, allowing for a more detailed analysis of their intrinsic properties.

ACKNOWLEDGEMENTS

This work is based on observations made with the NASA/ESA/CSA James Webb Space Telescope. We thank Dr. Daniel Eisenstein for the helpful discussion on JWST/JADES data. We acknowledge support by NASA ADAP Grant 80NSSC21K0637.

DATA AVAILABILITY

The data underlying this article will be shared on reasonable request to the corresponding author.

REFERENCES

- Adams N. J., et al., 2024, *ApJ*, **965**, 169
Atek H., et al., 2023a, *MNRAS*, **519**, 1201
Atek H., et al., 2023b, *MNRAS*, **524**, 5486
Austin D., et al., 2023, *ApJ*, **952**, L7
Bagley M. B., et al., 2023, *ApJ*, **946**, L12
Barkana R., Loeb A., 2001, *Phys. Rep.*, **349**, 125
Beckwith S. V. W., et al., 2006, *AJ*, **132**, 1729
Bhatawdekar R., Conselice C. J., Margalef-Bentabol B., Duncan K., 2019, *MNRAS*, **486**, 3805
Bolzonella M., Miralles J. M., Pelló R., 2000, *A&A*, **363**, 476
Bouwens R. J., et al., 2011, *ApJ*, **737**, 90
Bouwens R. J., et al., 2015, *ApJ*, **803**, 34
Bouwens R. J., et al., 2021, *AJ*, **162**, 47
Bradley L., et al., 2022, astropy/photutils: 1.5.0, doi:10.5281/zenodo.6825092
Bradley L., et al., 2023a, astropy/photutils: 1.10.0, doi:10.5281/zenodo.1035865
Bradley L. D., et al., 2023b, *ApJ*, **955**, 13
Brammer G. B., van Dokkum P. G., Coppi P., 2008, *ApJ*, **686**, 1503
Bromm V., Larson R. B., 2004, *ARA&A*, **42**, 79
Bromm V., Yoshida N., 2011, *ARA&A*, **49**, 373
Bruzual G., Charlot S., 2003, *MNRAS*, **344**, 1000
Bunker A. J., et al., 2023, *arXiv e-prints*, p. arXiv:2306.02467
Calzetti D., Armus L., Bohlin R. C., Kinney A. L., Koornneef J., Storchi-Bergmann T., 2000, *ApJ*, **533**, 682
Carnall A. C., McLure R. J., Dunlop J. S., Davé R., 2018, *MNRAS*, **480**, 4379
Castellano M., et al., 2022, *ApJ*, **938**, L15
Chatzikos M., et al., 2023, *Rev. Mex. Astron. Astrofis.*, **59**, 327
Chisholm J., et al., 2022, *MNRAS*, **517**, 5104
Ciesla L., Elbaz D., Fensch J., 2017, *A&A*, **608**, A41
Coe D., et al., 2019, *ApJ*, **884**, 85
Conroy C., Gunn J. E., 2010, FSPS: Flexible Stellar Population Synthesis, Astrophysics Source Code Library, record ascl:1010.043
Conroy C., Gunn J. E., White M., 2009, *ApJ*, **699**, 486
Curti M., et al., 2024, *A&A*, **684**, A75
Daddi E., et al., 2007, *ApJ*, **670**, 156
Dickinson M., Giavalisco M., GOODS Team 2003, in Bender R., Renzini A., eds, *The Mass of Galaxies at Low and High Redshift*. p. 324 (arXiv:astro-ph/0204213), doi:10.1007/10899892_78
Donnan C. T., et al., 2023, *MNRAS*, **518**, 6011
Duan Q., Conselice C. J., Li Q., Harvey T., Austin D., Ormerod K., Trussler J., Adams N., 2024, *MNRAS*, **529**, 4728
Eisenstein D. J., et al., 2023a, *arXiv e-prints*, p. arXiv:2306.02465
Eisenstein D. J., et al., 2023b, *arXiv e-prints*, p. arXiv:2310.12340
Elbaz D., et al., 2007, *A&A*, **468**, 33
Ellis R. S., et al., 2013, *ApJ*, **763**, L7
Fan X., Carilli C. L., Keating B., 2006, *ARA&A*, **44**, 415
Feroz F., Hobson M. P., 2008, *MNRAS*, **384**, 449
Finkelstein S. L., et al., 2015, *ApJ*, **810**, 71
Finkelstein S. L., et al., 2022, *ApJ*, **940**, L55
Finkelstein S. L., et al., 2023, *ApJ*, **946**, L13
Förster Schreiber N. M., Wuyts S., 2020, *ARA&A*, **58**, 661
Furtak L. J., Atek H., Lehnert M. D., Chevallard J., Charlot S., 2021, *MNRAS*, **501**, 1568
Furtak L. J., Shuntov M., Atek H., Zitrin A., Richard J., Lehnert M. D., Chevallard J., 2023, *MNRAS*, **519**, 3064
Giavalisco M., et al., 2004, *ApJ*, **600**, L93
Giménez-Arteaga C., et al., 2023, *ApJ*, **948**, 126
Grazian A., et al., 2015, *A&A*, **575**, A96
Hainline K. N., et al., 2020, *ApJ*, **892**, 125

- Hainline K. N., et al., 2024, [ApJ](#), **964**, 71
- Harikane Y., et al., 2023, [ApJS](#), **265**, 5
- Ishigaki M., Kawamata R., Ouchi M., Oguri M., Shimasaku K., Ono Y., 2015, [ApJ](#), **799**, 12
- Juodžbalis I., et al., 2023, [MNRAS](#), **525**, 1353
- Kroupa P., 2002, [Science](#), **295**, 82
- Laporte N., Meyer R. A., Ellis R. S., Robertson B. E., Chisholm J., Roberts-Borsani G. W., 2021, [MNRAS](#), **505**, 3336
- Larson R. L., et al., 2023, [ApJ](#), **958**, 141
- Leung G. C. K., et al., 2023, [ApJ](#), **954**, L46
- Lower S., Narayanan D., Leja J., Johnson B. D., Conroy C., Davé R., 2020, [ApJ](#), **904**, 33
- Mason C. A., Trenti M., Treu T., 2023, [MNRAS](#), **521**, 497
- McLeod D. J., McLure R. J., Dunlop J. S., 2016, [MNRAS](#), **459**, 3812
- Morales A. M., et al., 2024, [ApJ](#), **964**, L24
- Naidu R. P., et al., 2022, [ApJ](#), **940**, L14
- Nakajima K., Ouchi M., Isobe Y., Harikane Y., Zhang Y., Ono Y., Umeda H., Oguri M., 2023, [ApJS](#), **269**, 33
- Noeske K. G., et al., 2007, [ApJ](#), **660**, L43
- Nonino M., et al., 2023, [ApJ](#), **942**, L29
- Oesch P. A., et al., 2016, [ApJ](#), **819**, 129
- Oke J. B., Gunn J. E., 1983, [ApJ](#), **266**, 713
- Ouchi M., Ono Y., Shibuya T., 2020, [ARA&A](#), **58**, 617
- Planck Collaboration et al., 2020, [A&A](#), **641**, A6
- Plat A., Charlot S., Bruzual G., Feltre A., Vidal-García A., Morisset C., Chevallard J., Todt H., 2019, [MNRAS](#), **490**, 978
- Pontoppidan K. M., et al., 2022, [ApJ](#), **936**, L14
- Popesso P., et al., 2023, [MNRAS](#), **519**, 1526
- Rieke M. J., Kelly D., Horner S., 2005, in Heaney J. B., Burriesci L. G., eds, Society of Photo-Optical Instrumentation Engineers (SPIE) Conference Series Vol. 5904, Cryogenic Optical Systems and Instruments XI. pp 1–8, doi:10.1117/12.615554
- Rieke M. J., et al., 2023a, [PASP](#), **135**, 028001
- Rieke M. J., et al., 2023b, [ApJS](#), **269**, 16
- Rigby J., et al., 2023, [PASP](#), **135**, 048001
- Robertson B., et al., 2023, [arXiv e-prints](#), p. arXiv:2312.10033
- Salmon B., et al., 2015, [ApJ](#), **799**, 183
- Salmon B., et al., 2020, [ApJ](#), **889**, 189
- Sarkar A., Samui S., 2019, [PASP](#), **131**, 074101
- Schenker M. A., et al., 2013, [ApJ](#), **768**, 196
- Scoville N., et al., 2007, [ApJS](#), **172**, 1
- Speagle J. S., Steinhardt C. L., Capak P. L., Silverman J. D., 2014, [ApJS](#), **214**, 15
- Stark D. P., 2016, [ARA&A](#), **54**, 761
- Tacchella S., et al., 2023, [MNRAS](#), **522**, 6236
- Treu T., et al., 2022, [ApJ](#), **935**, 110
- Windhorst R. A., et al., 2023, [AJ](#), **165**, 13
- Witten C. E. C., Laporte N., Katz H., 2023, [ApJ](#), **944**, 61
- Yang L., et al., 2022, [ApJ](#), **938**, L17

This paper has been typeset from a \LaTeX file prepared by the author.